

# Materials Horizons

Accepted Manuscript

This article can be cited before page numbers have been issued, to do this please use: E. Di Lorenzo, L. Miele, A. Longo, E. Di Maio and M. L. Di Lorenzo, *Mater. Horiz.*, 2026, DOI: 10.1039/D6MH00281A.



This is an Accepted Manuscript, which has been through the Royal Society of Chemistry peer review process and has been accepted for publication.

Accepted Manuscripts are published online shortly after acceptance, before technical editing, formatting and proof reading. Using this free service, authors can make their results available to the community, in citable form, before we publish the edited article. We will replace this Accepted Manuscript with the edited and formatted Advance Article as soon as it is available.

You can find more information about Accepted Manuscripts in the [Information for Authors](#).

Please note that technical editing may introduce minor changes to the text and/or graphics, which may alter content. The journal's standard [Terms & Conditions](#) and the [Ethical guidelines](#) still apply. In no event shall the Royal Society of Chemistry be held responsible for any errors or omissions in this Accepted Manuscript or any consequences arising from the use of any information it contains.



foamlab

foaming laboratory at University of Naples Federico II

Online  
DOI: 10.1039/C6MH00281A

**New concepts statement,** “Time-Temperature-Transformation-Layering diagrams: a design tool for lightweight multi-layered, single-material polymeric structures”.

This work introduces a framework for designing mono-material, multi-layered structures within a single component, eliminating the need for melt bonding, soldering, or adhesives while enhancing performance, sustainability, and manufacturing simplicity. The central advance lies in redefining Time-Temperature-Transformation (TTT) diagrams, which traditionally describe transformation kinetics under spatially uniform conditions and provide no guidance for spatial structuring. Here, transport bands are superimposed onto TTT diagrams to incorporate the characteristic length and time scales of heat and/or mass transport, identifying regions where transport rates are comparable to transformation kinetics over a defined depth. This transforms the classical TTT diagram into a spatio-temporal design map that enables the deliberate formation of layered architectures within a single material. Polymers serve as model systems, with poly(lactic acid) and poly(ethylene terephthalate) subjected to combined pressurized carbon dioxide and thermal treatments, producing controlled variations in structure and density from initially amorphous samples in a single processing step. More broadly, the framework establishes a generalizable principle for coupling transport phenomena with phase transformation kinetics, offering a versatile conceptual tool for research and materials engineering education.

Naples, Italy, April 3, 2026.

Ernesto Di Maio





foamlab

foaming laboratory at University of Naples Federico II

Online  
DOI: 10.1039/C6MH00281A

## Data Availability Statement

The data that support the findings of this study are openly available on figshare, <https://figshare.com/s/b1b75594bf0fd1a3adae>.

Naples, Italy, February 13, 2026.

Ernesto Di Maio  


Materials Horizons Accepted Manuscript



Cite this: DOI: 00.0000/xxxxxxxxxx

# Time-Temperature-Transformation-Layering diagrams: a design tool for lightweight multi-layered, single-material polymeric structures

Emilia Di Lorenzo<sup>a,b†</sup>, Lorenzo Miele<sup>a,b†</sup>, Alessandra Longo<sup>c\*</sup>, Ernesto Di Maio<sup>a,b\*</sup>, Maria Laura Di Lorenzo<sup>c</sup>Received Date  
Accepted Date

DOI: 00.0000/xxxxxxxxxx

In the *design for recycling* strategy, reducing the number of different materials is encouraged. However, multi-material structures like multi-layers are often used to optimize performance. Here, we demonstrate that by engineering the coupled mass and heat transport during the processing of semi-crystalline polymeric components, it is possible to achieve a multilayered structure using a single material. Layering — in terms of crystallinity and foaming — has been accomplished by identifying the processing window in which the characteristic times are of the same order of magnitude for: (i) mass transport of the foaming agent in the polymer, (ii) heat transport and (iii) polymer crystallization. A time-temperature-transformation-layering diagram is thus constructed and exploited. This strategy has been validated using two different semi-crystalline polymers, poly(lactic acid) and poly(ethylene terephthalate), and CO<sub>2</sub> as foaming agent. We demonstrate that sustainability and performance need not be mutually exclusive. Possibility of leveraging this approach with other types of materials and/or processes for which layering is required significantly broadens the scope of this research.

## 1 Introduction

Materials layering is the prevalent strategy for optimizing structural and functional performance, commonly observed in both natural and artificial systems<sup>1–3</sup>. From a structural perspective, layering is often employed to address the conflict between strength and toughness, as these are equally vital requirements; however, they are generally mutually exclusive<sup>4</sup>. Sandwich structures, formed by a low-density core — in some cases a foam — and high-stiffness, fiber-reinforced composite outer layers, are examples of this nature-mimicking, performance-improving strategy, and are found in advanced applications such as wind turbines, boats, and aircraft<sup>5</sup>. From a functional perspective, multi-layer structures are utilized in electronics, electromagnetic shielding, sensing, packaging, energy, medicine, pharmaceuticals, etc. However, in functional applications, the necessity for an active layer and the high added value of typical products may limit the

relevance of the present study.

The intimately bonded coexistence of different materials in multi-layer systems makes their recycling, both mechanical and chemical, extremely challenging. Within the *design for recycling* approach, mono-material systems are strongly preferred over multi-material ones<sup>6–8</sup>. In mono-material layered systems, different properties can be achieved through variations in composition, structure (e.g., orientation, crystallinity), and fine-tuning of additives (e.g., 2D materials to enhance barrier properties in packaging)<sup>9</sup>. The search for suitable material solutions is currently vibrant and diverse, with innovative and creative strategies aimed at matching the performance of multi-material systems<sup>10–12</sup>. However, from a processing standpoint, a comparable effort appears to be lacking in the development of simplified technologies that address the need for improved sustainability and recyclability of products.

In this context, some of the authors introduced the concept of time-varying boundary conditions in (i) mass and (ii) heat transport problems during processing to achieve layering. These were applied respectively to (1) polymer foaming<sup>13</sup> and (2) egg cooking<sup>14,15</sup>. In particular, in reference<sup>13</sup>, multi-graded foams were obtained by imposing a pressure treatment with a characteristic time  $t_p$  on the order of the mass transport characteristic time,  $\tau_m = L^2/D$ , where  $L$  is the characteristic size of the part and  $D$  is the mutual diffusivity of the polymer/foaming agent system.

<sup>a</sup> Dipartimento di Ingegneria Chimica, dei Materiali e della Produzione Industriale, University of Naples Federico II, Piazzale Vincenzo Tecchio, 80, Naples, 80125, Italy.

<sup>b</sup> foamlab, University of Naples Federico II, Piazzale Vincenzo Tecchio, 80, Naples, 80125, Italy.

<sup>c</sup> Institute of Polymers, Composites and Biomaterial, Via Campi Flegrei, 34, Pozzuoli (NA), 80078, Italy.

† These authors contributed equally to this work.

\* Corresponding authors. Email addresses: edimaio@unina.it (E. Di Maio), alessandra-longo@cnr.it (A. Longo)



This pressure treatment induces a non-equilibrium foaming agent concentration profile,  $c = c(x, t)$ . Upon an instantaneous pressure release (i.e., with a characteristic time  $t_f \ll t_p$ ) at a given time  $\bar{t}$ , foaming is achieved. In some sense, the pressure release "writes" the concentration profile  $c = c(x, \bar{t})$ . Notably, the resulting foam exhibits a lower density and a higher bubble number density in regions ( $x$ ) where  $c$  is larger.

In reference<sup>14</sup>, the same concept was applied to induce layering in eggs, allowing for the cooking of the albumen and the yolk at two different temperatures (the optimal cooking temperatures are 65°C for the yolk and 85°C for the albumen). Again, by using a temperature treatment with a characteristic time  $t_T$  on the order of the heat transport characteristic time,  $\tau_h = L^2/a$ , where  $a$  is the thermal diffusivity of the albumen, a non-equilibrium temperature profile  $T = T(x, t)$  is induced. Unlike the previous case, in cooking (as well as in other temperature treatments that induce material changes, such as curing or crystallization in polymers), the instantaneous temperature profile  $T = T(x, \bar{t})$  is not sufficient to establish a cooking degree profile, as cooking requires time. A characteristic time can be defined here, for example, as the half-time of the cooking reaction to completion,  $\tau_X(T) = 1/k$ , where  $k$  is the reaction kinetics constant. Time integration of the reaction kinetics yields the degree of cooking. In this case, as the temperature profile evolves over time, one must be inventive in designing temperature treatments that meet the desired objectives. In reference<sup>14</sup>, the authors introduced *periodic cooking* as the treatment to fully cook the yolk and albumen, where a number  $N$  of high-temperature and low-temperature cooking cycles were applied, with  $N = \tau_X/\tau_h$ .

The concurrent use of the two aforementioned transport phenomena is employed here to induce layering in both the density and the degree of crystallinity in slabs of two model polymers: poly(lactic acid) (PLLA) and poly(ethylene terephthalate) (PET). Mono-material, multi-layered parts are thus designed and processed in a single step during pressure release, following a well-defined heat and pressure treatment.

We therefore demonstrate how knowledge of the combined interaction of transport phenomena and phase transformations during material processing allows for an accurate, unprecedented prediction of the final morphology. A graphic tool (a time, temperature, transformation, and layers - TTTL - map) is proposed to visualize the idea and verify the available processing windows to achieve the desired layered structure. Possible extensions to any material and treatment type are suggested and encouraged.

## 2 Materials and Methods

### 2.1 Materials

Amorphous PLLA grade Lx175, with a melt flow index (210°C/2.16 kg) of MFI = 6 and 4% D-isomer units, was kindly provided by Total Corbion (Gorinchem, The Netherlands). PET M4 P80 was kindly received from PointPlastic S.r.l. (Amasona, Italy).

The PLLA and the PET were first dried at 60°C under vacuum overnight and then shaped into sheets of 2.0 and 1.5 mm thickness, respectively, via compression molding, followed by rapid

quenching to ambient temperature to hinder crystal formation. In both cases, disks of 5 mm diameter were formed by punching from the sheets. In the case of PLLA, slabs with  $W \times T \times L = 18 \times 2 \times 100 \text{ mm}^3$  were also produced from the sheets for the three point bending tests.

CO<sub>2</sub> (purity 99.99%) was purchased from SOL S.p.A. (Monza, Italy).

### 2.2 Methods

#### 2.2.1 Physical foaming experiments

Physical foaming of the PLLA and PET slabs in the shape of disks with  $L = 1 \text{ mm}$  was performed in a custom-made pressure vessel, thoroughly described elsewhere<sup>16</sup>, designed to allow the fine-tuning of all the foaming variables (temperature, pressure, and pressure drop rate (PDR)). Before the actual experiment, the vessel was pre-heated to the desired temperature to prevent possible effects of the heating ramp on the polymer microstructure build-up (i.e., cold crystallization). Once the desired temperature was reached (ranging from 45 to 120 °C in the case of PLLA and from 70 to 260 °C in the case of PET), the foaming experiment was initiated by loading one PLLA (or PET) disk into the vessel and subsequently increasing the pressure up to 110 bar of CO<sub>2</sub>. The lower temperature limit of the processing window is related to the glass transition temperature ( $T_g$ ), which is  $T_g = 60 \text{ °C}$  for PLLA<sup>17</sup> and  $T_g = 69 \text{ °C}$  for PET<sup>18</sup>, also taking into account the plasticizing effect of CO<sub>2</sub><sup>17,19</sup>. The upper temperature relates to the melting points of the two polymers, as quantified in reference<sup>20-23</sup> for PLLA, and in reference<sup>18</sup> for PET.

The pressure was then maintained constant for a time of  $t_p = 2, 5, 10, 20, 40 \text{ min}$  in the case of PLLA and  $t_p = 2, 30 \text{ min}$  in the case of PET. Finally, the pressure was rapidly released over a time period of  $t_f \ll t_p$ , and the foamed sample was removed from the reactor and stored at room temperature. In the case of PET, a non-isothermal treatment was also attempted, involving (i) loading the sample into the pre-heated pressure vessel at  $T = 260 \text{ °C}$ , (ii) increasing the CO<sub>2</sub> pressure up to 110 bar, and (iii) continuous cooling of the pressure vessel down to 220 °C over a time span of 8 min before pressure quenching. For the PLLA slabs of  $W \times T \times L = 18 \times 2 \times 100 \text{ mm}^3$ , the same foaming procedure was followed, but a pressure vessel characterized by a larger internal volume was used, as fully detailed in reference<sup>24</sup>.

#### 2.2.2 Microscopy

The foamed samples were extracted from the vessel and characterized in terms of morphology by optical microscopy. The treated samples were cut in half using an ultra-thin stainless steel blade, and their morphology was observed using an optical microscope (Stemi 508, Zeiss, Oberkochen, Germany). The thickness of each visible layer in the cross section was quantified using the ImageJ software (in the best case, this included a crystalline skin, a foamed part, and the unfoamed core of the sample). The thickness of the saturated layer ( $x$ ) was determined by evaluating the difference between the initial thickness of the sample and the core thickness. From this, the polymer/foaming agent (hereafter referred to as gas) mutual diffusivity at different temperatures was

149 estimated as follows:

$$D \approx \frac{x^2}{t_p} \quad (1)$$

150 This procedure was followed equally for PLLA and PET, allow-  
151 ing us to retrieve the light red diamonds of Figure 1. In fact,  
152 even minor variations in material characteristics, such as molec-  
153 ular weight polydispersity, can result in significant differences in  
154 the physical properties of the polymer. Therefore, for accurate  
155 and quantitative processing design, specific material analysis may  
156 be required.

157 On the other side, the treated samples were also analyzed with  
158 a Zeiss Axioskop polarized optical microscope (POM), equipped  
159 with a CFW-1312C Digital Camera (Scion Corporation, Maryland,  
160 USA). Images were captured with the Image-Pro Plus 7.0 software  
161 (Media Cybernetics). The foams were embedded in resin and cut,  
162 parallel to the direction of the characteristic length, into 30  $\mu\text{m}$   
163 thick slices by means of a cryomicrotome (Olimpus DP 21, Tokyo,  
164 Japan) at  $-20\text{ }^\circ\text{C}$ . The resulting slices were placed on glass slides  
165 and carefully washed with water to remove the resin before POM  
166 imaging. This procedure was only followed for PLLA (Figure 2  
167 and Figure 5).

### 168 2.2.3 Thermal analysis

169 The thermal properties and crystallization kinetics of the samples  
170 were investigated using a PerkinElmer (Massachusetts, United  
171 States) Pyris Diamond Differential Scanning Calorimeter (DSC),  
172 equipped with an Intracooler II as a cooling system, in isothermal  
173 mode by varying the cold crystallization temperature. Temper-  
174 ature and energy calibration were performed with a high purity  
175 indium standard. Dry nitrogen gas was used to purge the sample  
176 environment at a flow rate of 30 mL/min. All experiments were  
177 repeated three times to ensure reproducibility. Each heating scan  
178 was performed from 0 to 200  $^\circ\text{C}$  at a rate of 20  $^\circ\text{C}/\text{min}$ . To ob-  
179 tain accurate heat capacity data from the heat flow rate measure-  
180 ments, each scan was paired with a reference run using an empty  
181 pan, with the masses of the aluminum sample pan and the refer-  
182 ence pan matched within 0.03 mg. More details are presented in  
183 reference<sup>25</sup>.

### 184 2.2.4 Atomic force microscopy

185 Stiffness mapping of the three-layered PLLA slabs was performed  
186 using atomic force microscopy (AFM); a PLLA foamed sample  
187 was cut into a sub-millimeter thick slice with an ultra-thin stain-  
188 less steel blade. An inverted optical microscope (Olympus IX71,  
189 Tokyo, Japan) equipped with a 10x objective (Olympus PLN 10x,  
190 Tokyo, Japan) was integrated with an AFM instrument (NTMDT  
191 NTEGRA Prima, Sutton, The Netherlands) to position the AFM  
192 head directly on top of the optical microscope, thereby allowing  
193 observation of the slab during the testing procedures<sup>26</sup>. A silicone  
194 probe with a nominal cantilever spring constant ranging between  
195 0.01-0.5 N/m (CSG10, TipsNano, Tallinn, Estonia) was used for  
196 mapping stiffness in contact mode over an area of 64 x 64  $\mu\text{m}$   
197 both in the core and the outer layer of the sample (Figure 2).

### 198 2.2.5 Three-points bending tests

199 Bending tests were carried out in a three-point bending test con-  
200 figuration using the MTS Alliance RT/50 (Eden Prairie, Min-  
201 nesota, USA) universal testing machine equipped with a load cell  
202 of 50 kN. The span was fixed at 50 mm, and a displacement rate  
203 of 5.0 mm/min was adopted. For each sample, three specimens  
204 were manufactured and tested. The bending stiffness was evalu-  
205 ated as the initial slope of the force-displacement curve, and the  
206 fracture energy was determined as the area beneath the entire  
207 curve. All samples had the same initial weight.

## 208 3 Results

209 Literature data<sup>27-36</sup> about the effect of temperature on thermal  
210 and mass diffusivities, as well as on crystallization under  $\text{CO}_2$   
211 for PLLA, can be compared to infer the possibility of designing  
212 treatments that induce the formation of layers endowed with dif-  
213 ferent degrees of crystallinity and/or foaming. These data were  
214 collected and processed to derive the characteristic times of mass  
215 and heat transport and of crystallization ( $\tau_m$ ,  $\tau_h$ ,  $\tau_X$ , as defined  
216 in the Introduction). Characteristic dimensions spanning three  
217 orders of magnitude ( $L = 0.1, 1$  and 10 mm) were considered for  
218 the calculation. The corresponding rates of mass and heat trans-  
219 port and of crystallization were then derived as the respective  
220 reciprocals ( $1/\tau_m$ ,  $1/\tau_h$ ,  $1/\tau_X$ ), and their comparison is shown in  
221 Figure 1, which reports data referring to PLLA grades containing  
222 4% of D-isomer with molar weight ranging between 40 and 200  
223 kDa. The latter range was selected based on literature knowledge  
224 on the influence of main parameters (molecular weight, melt flow  
225 index, stereoregularity) on crystallization of PLLA<sup>37-40</sup>. More-  
226 over, we considered overall crystallization rates, which take into  
227 account both crystal nucleation and growth rates, for various  $\text{CO}_2$   
228 pressure, due to its huge effect on crystallization of PLLA<sup>19</sup>.

229 As it is visible, the rate of heat transport is relatively constant  
230 in the reported experimental range, while the rate of mass trans-  
231 port increases exponentially with temperature, as is typically re-  
232 ported in the literature. The crystallization rate, on the other  
233 hand, exhibits non-monotonic behavior with temperature, show-  
234 ing the characteristic bell shape<sup>22</sup>, and is massively affected by  
235 sorption of high pressure  $\text{CO}_2$ <sup>32,36,41-43</sup>, due to the  $\text{CO}_2$  plas-  
236 ticization effect<sup>44</sup>. Indeed, the dissolved gas increases the mo-  
237 bility of the polymer chains and, consequently, it determines an  
238 increase in the rate of crystallization<sup>45</sup>. This behavior is evident  
239 from the blue, cyan, and pink data in Figure 1<sup>32</sup>, showing that the  
240 crystallization rate peak not only increases but also shifts towards  
241 lower temperature values as the  $\text{CO}_2$  pressure is progressively in-  
242 creased, and this is valid for both cold and melt crystallization.

243 The shift, which is here shown up to 45 bar of  $\text{CO}_2$ , is expected  
244 to be enhanced at higher pressures, compatibly with the increased  
245 amount of gas sorbed<sup>45</sup>. This will be taken into account later in  
246 this article to allow for validation of the experimental campaign  
247 conducted at 110 bar. In the general case of lack of data in the  
248 literature, this shift can be assessed relying on well-established  
249 theoretical predictions<sup>46-48</sup>. Figure 1 allows us to design a treat-  
250 ment to achieve structure and density layering: once the charac-  
251 teristic dimension of the sample of interest is known, the user can

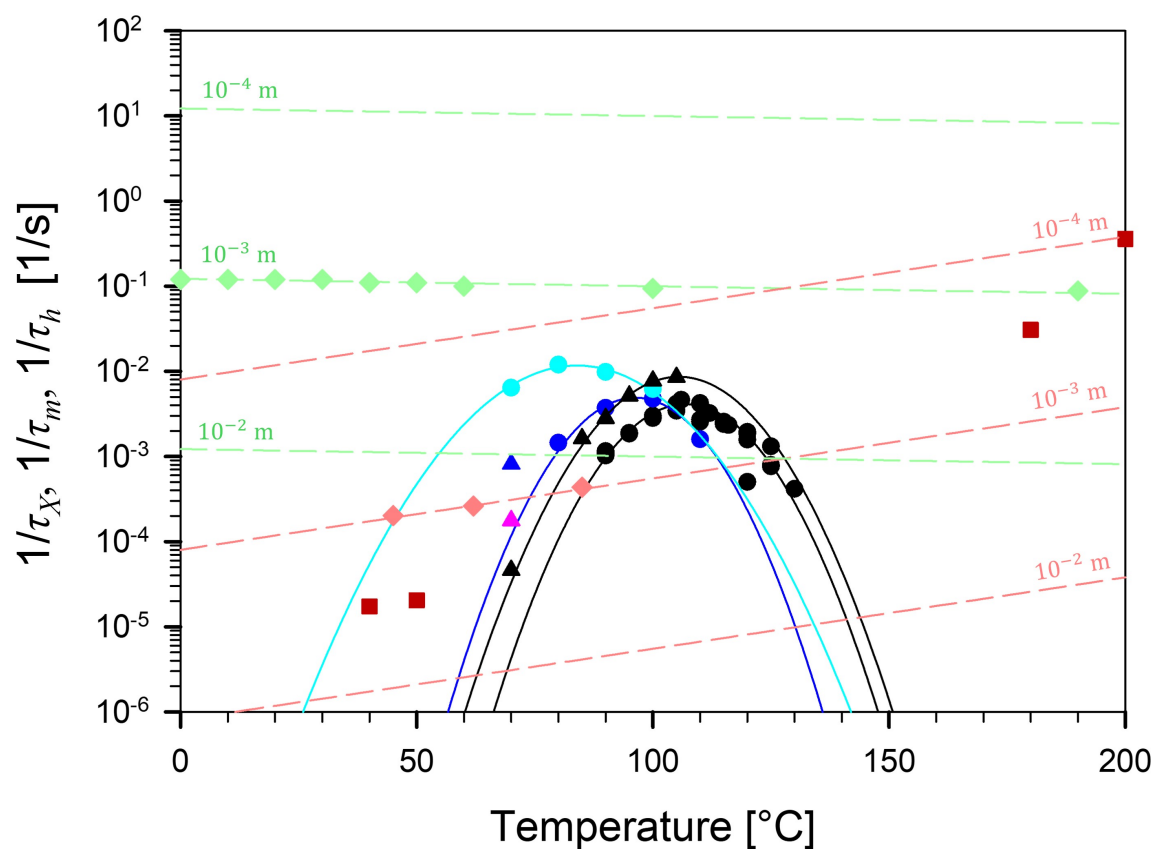


Fig. 1 Comparison of the rates of the three concurring phenomena for the system PLLA/CO<sub>2</sub>.  $1/\tau_m = D/L^2$  is the rate of mass transport (full dark red squares were taken from<sup>27–30</sup>, while light red diamonds are our data);  $1/\tau_h = a/L^2$  (green diamonds) is the rate of heat transport<sup>31</sup>;  $1/\tau_X$  is the crystallization rate, evaluated as the reciprocal of the half-time of crystallization. The latter is presented as a function of CO<sub>2</sub> pressure: black, blue and cyan circles indicate  $1/\tau_X$  at ambient pressure<sup>32–35</sup>, with 15 bar of CO<sub>2</sub><sup>32</sup> and with 45 bar of CO<sub>2</sub><sup>32</sup>, respectively, in the case of melt crystallization; similarly, black, pink and blue triangles indicate  $1/\tau_X$  at ambient pressure<sup>34,36</sup>, with 5 bar of CO<sub>2</sub><sup>36</sup> and with 20 bar of CO<sub>2</sub><sup>36</sup> in the case of cold crystallization. A value of  $L = 0.1, 1$  and  $10$  mm was used for the evaluation of  $1/\tau_m$  and  $1/\tau_h$ . Lines are used as a guide to the eye. In all cited references, PLLA has a D-isomer content of 4% and a molecular weight ranging between 40 and 200 kDa.

leverage the direct comparison between the occurring phenomena to understand the appropriate processing conditions for this purpose. In the case of a 2 mm slab of PLLA ( $L = 1$  mm), the high rate of heat transport (green lines) hinders the use of thermal treatments as a means to induce material structure layering, since the temperature quickly equilibrates within the given sample (temperature can be considered uniform). The design of the process may then be restricted to the sole exploitation of polymer crystallization and CO<sub>2</sub> diffusion, which have comparable rates in the temperature range of 40 to 140 °C, where structure and density layering appear feasible. To validate this approach, a batch foaming experiment was conducted at 45 °C. A slab of amorphous PLLA ( $L = 1$  mm) was treated with 110 bar of CO<sub>2</sub> for  $t_p = 20$  min, and then pressure quenched with  $t_f = 0.1$  s for foaming.

The optical microscopy of the cross section of the resulting sample is presented in Figure 2a. A multilayer structure can be recognized: as we move from the skin towards the core of the sample, we encounter, in sequence, a dense layer, a foamed layer, and another dense, compact layer in the exact center of the slab. The thermal analysis (Differential scanning calorimetry), as fully de-

tailed in reference<sup>25</sup>, reveals the nature of the dense layers, indicating a difference in the degree of crystallinity, which is 0.23 for the outer layer and 0.02 for the central layer. This difference is also confirmed by the POM micrograph of Figure 2b, which reveals the presence of round, bright elements, typical of spherulite formations, in the outer layer, but not in the core, which remains dark: optical isotropy is evidenced here, as characteristic of amorphous material<sup>49,50</sup>. AFM stiffness mapping (Figure 2c) also confirms the physical state of the two layers. A uniform stiffness value of approximately 0.037 mN/μm is measured in the amorphous area (A), while a bimodal distribution of stiffness values is detected in the outer layer (X), with the modes being 0.023 and 0.057 mN/μm, again evidencing the presence of stiff crystalline domains within a soft amorphous matrix<sup>51–53</sup>.

This result is fully compatible with expectations arising from the qualitative analysis of Figure 1. When the amorphous PLLA slab is placed in the autoclave at 45 °C, the crystallization rate is uniformly negligible (the black curve lies above 45 °C). As the sample comes into contact with CO<sub>2</sub> during pressurization, the gas diffuses into the system at a rate of  $1/\tau_m > 1/\tau_X$ . How-



ever, as the gas penetrates the PLLA slab, the crystallization rate curve increases locally (cyan curve), and  $1/\tau_X$  begins to approach  $1/\tau_m^{45}$ . As a consequence, a front of crystallinity appears, which lags behind the diffusive front of  $\text{CO}_2$  penetrating inside the polymer. At pressure quench, we are able to freeze these two chasing fronts: within the  $\text{CO}_2$  penetration depth, only the non-crystallized layer is allowed to expand, and if the front has not passed through the whole sample, the presence of three different layers is highlighted, just as previously described: an amorphous core, a foamed layer, and a crystalline skin.

This successful experiment confirms the possibility of exploiting Figure 1 as a source of information for material and process design. Indeed, Figure 1 can be used as a starting point to obtain a proper Time-Temperature-Transformation-Layering (TTTL) diagram that the user can leverage as a guide to understand the interplay between the concurrent phenomena occurring inside the sample and, consequently, to predict the resulting sample morphology. The TTTL diagram for a slab of PLLA with  $L = 1$  mm, in which a layering with a characteristic dimension  $\delta$  of 0.1 mm is desired, is fully shown in Figure 3a. Here, consistent with the quick heat transport, we omitted the corresponding curves.

Concerning the rate of gas diffusion ( $1/\tau_m$ ), two lines were selected: the first one ( $1/\tau_m^\delta$ ) was evaluated considering  $\delta = 0.1$  mm, while the second one ( $1/\tau_m^L$ ) was evaluated considering  $L = 1$  mm. These two lines together approximately mark the beginning and end of the diffusion phenomenon in the sample. The bell-shaped curves of the crystallization rate of PLLA in the absence of  $\text{CO}_2$  and with  $\text{CO}_2$  (at the pressure value corresponding to the desired experimental condition) delineates the pink areas. The latter evidence the regions in which crystallization is allowed to occur, either at ambient or high pressure, and are specifically modified to better depict their interaction with gas diffusion. An additional bell-shaped curve is also represented, just below  $1/\tau_m^L$ , as an indicator of the crystallization occurring when the processing time  $t_p$  is long enough to fully crystallize the sample. Superimposition of the modified kinetic curves, in coherence with the presented discussion, highlights the presence of six different regions: given the processing conditions (temperature and time), the final sample can result in being fully amorphous (A), fully crystalline (X), fully foamed (F), or, as in the previously reported case, layered; i.e., a combination of the aforementioned (either F+A, X+F, or X+F+A). In other words, layering only arises when the system undergoes transformation under non-uniform chemical potential fields.

In order to generalize the concept, the possibility for inducing layering can be rapidly assessed using the Damköhler number ( $Da = \tau_m/\tau_{1/2}$ ), directly relating the transformation rate to the transport rate, specifically in the region in which layering is desired ( $\delta$ ). Given the processing conditions (time, temperature and thickness), only when  $Da_\delta \approx 1$  layering arises.

To better understand the potential of this diagram in the laboratory or industrial practice of batch foaming, a series of case studies is also presented (Figure 3b). Here, on each TTTL diagram, the duration of the treatment is depicted as an arrow: when the arrow crosses a kinetic curve, the corresponding transformation occurs inside the system; the final sample morphology is deter-

mined by the final region reached by the arrow.

In case (I), the arrow does not cross any kinetic curve and remains confined in region (A), meaning that no transformation occurs and the sample stays amorphous; this happens at any temperature when  $t_p < \tau_m^\delta$ .

In case (II), the arrow only crosses the first diffusion curve but not the second one or any crystallization curve, reaching the (F+A) region; this occurs when  $\tau_m^\delta < t_p < \tau_m^L$  and, if in the temperature range where crystallization is enabled ( $45 < T < 120$  °C),  $t_p > \tau_X$ . In this instance, the temperature does not favor crystallization, and the processing time is long enough to allow diffusion in just a portion of the sample, which, upon pressure release, results in only partial foaming.

In case (III), the arrow crosses both the diffusion curves but not the crystallization curves, reaching the (F) region; this occurs when  $t_p > \tau_m^L$  and the temperature does not enable sample crystallization ( $T < 35$  °C or  $T > 135$  °C, approximately). In this instance, the final sample, upon pressure quenching and thanks to gas uptake, is fully foamed.

Case (IV) is the most interesting one. Here, the arrow crosses both the first diffusion curve and the high pressure crystallization curve, reaching the (X+F+A) region. This can only happen when  $t_p > \tau_m^\delta$  and  $t_p > \tau_X$ , given that the temperature is sufficient to activate  $\text{CO}_2$ -induced crystallization (again  $45 < T < 120$  °C). As a consequence, the portion of the sample that is not reached by the gas remains amorphous, while the other portion undergoes gas-induced crystallization in the form of a front lagging behind the diffusion front. Overall, upon pressure release, a three-layered structure is formed, with an amorphous core, a foamed part, and a crystalline skin. The example presented in Figure 2 fits into this case.

In case (V), the arrow not only crosses the diffusion curves but also the crystallization curves, falling in the (X) region. This happens when  $t_p > \tau_m^L$  in the temperature range where crystallization is allowed, whether simple or gas-induced. The combination of such temperatures and processing times allows for thorough crystal formation, and the final sample is fully crystalline.

Finally, case (VI) shows intermediate behavior between case (IV) and case (V). Here, the arrow crosses the first diffusion curve and both crystallization curves (i.e., temperature favors crystallization and, concomitantly,  $\tau_m^\delta < t_p < \tau_m^L$ ), reaching region (X+F). Accordingly, the portion of the sample reached by the gas undergoes gas-induced crystallization (with a crystallization front lagging behind the diffusion front), while the other portion, differing from case (IV), fully crystallizes, being in the region where crystallization without  $\text{CO}_2$  is also promoted. The final morphology features a two-layered structure, with a foamed part surrounded by crystals.

An experimental campaign aimed at validating the TTTL diagram was conducted on slabs of PLLA ( $L = 1$  mm). The explored processing conditions, together with the optical micrographs of the cross sections of the resulting samples, are shown in Figure 4. These are directly overlaid on the zoomed-in TTTL diagram to demonstrate the analogy between expected and experimental results. As visible, a good correspondence can be found at  $T = 62, 85$  and  $120$  °C for all processing times, as the three-layered structure

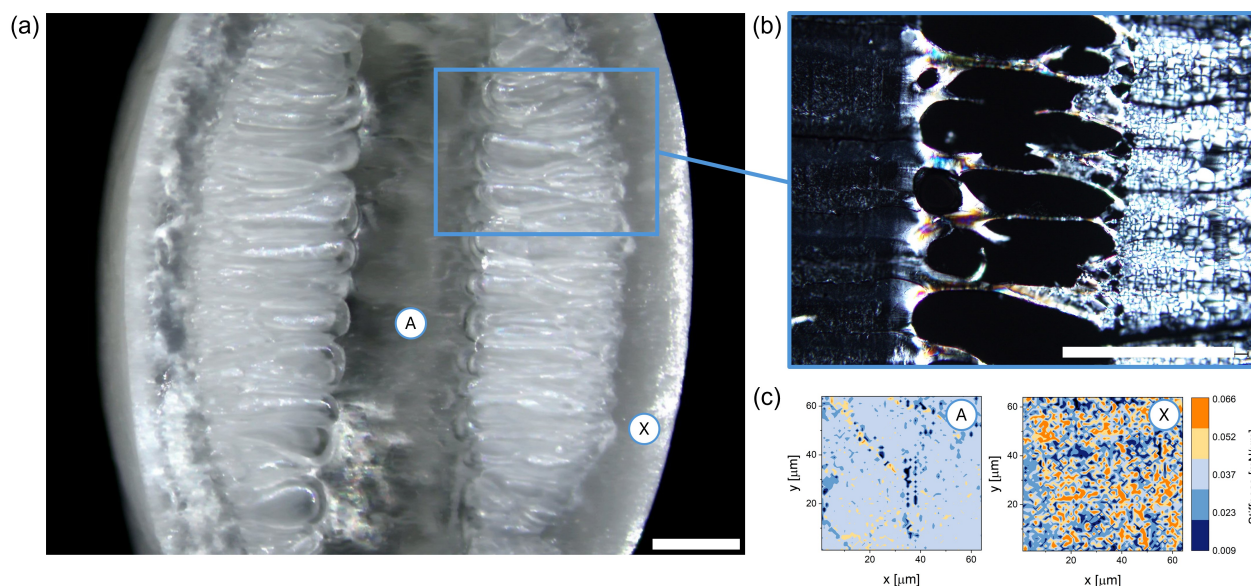


Fig. 2 (a) Optical microscopy image of a cross section of a PLLA sample treated at high pressure of CO<sub>2</sub>; (b) cross-polarized optical micrograph of a 30 μm thick slice of PLLA in the transition region from core to skin, and (c) AFM stiffness mapping in a 64 × 64 μm region in the core (A) and the skin (X) of the foamed PLLA sample. Scale bar = 500 μm in both (a) and (b).

only appears in the light pink region (X+F+A). Conversely, when outside of it (dark gray region), only two-layers are visible, as the conditions to initiate crystallization are not yet met. Some discrepancies are found only in the samples treated at  $T = 45\text{ }^{\circ}\text{C}$ , specifically for longer processing times ( $t_p = 10, 20, 40\text{ min}$ ). This is likely due to the fact that the high pressure crystallization kinetics were retrieved from literature data collected at 45 bar of CO<sub>2</sub>, while our experiments were conducted with 110 bar of CO<sub>2</sub>, a much higher value. As already discussed, the actual crystallization kinetics at such a high pressure is even more shifted toward lower temperature values, and the (X+F+A) region can be extended accordingly, as exemplified in Figure 4 with the dashed line<sup>17</sup>.

As a final remark, scale-up was successfully performed. Indeed, to prove the beneficial effect of layering on mechanical performance, we produced PLLA slabs with a geometry suitable for three point bending tests ( $W \times T \times L = 18 \times 2 \times 100\text{ mm}^3$ ). The resulting samples and the corresponding optical and POM microphotographs are shown in Figure 5. Regarding the mechanical properties, with respect to the totally crystalline beam (X), the (X+F+A) sandwich showed a slight reduction in bending stiffness (-12%) but a remarkable increase in fracture energy (+210%), due to the presence of the tougher amorphous and foamed core (Figure 5c). The possibility of improving performance in a single-material, sustainable part was thus demonstrated.

This very interesting and promising result lays the foundation for a new approach to batch foaming, not only of PLLA but also of any semi-crystalline polymer. An example of how the TTTL diagram can appear in the case of PET is shown in Figure 6, where literature data<sup>18,45,48,54–60</sup> on thermal and mass diffusivities, as well as on PET crystallization under CO<sub>2</sub>, are compared to assess the feasibility of designing treatments for material layering,

similarly to what was done for PLLA. The corresponding TTTL diagram for a slab of polymer with  $L = 1\text{ mm}$  is presented in Figure 6b, highlighting a completely different picture, as new challenges and possibilities arise when changing the polymer.

It is evident that, in this instance, the possibility of obtaining a layered structure still exists; however, due to the less effective CO<sub>2</sub> plasticizing effect, much smaller (X+F) and (X+F+A) regions are identified, implying a higher intrinsic difficulty in the layering of PET through isothermal treatments in comparison to PLLA.

This is also evident from Figure 7a, where, similarly to Figure 4, the optical micrographs of the cross sections of processed PET slabs ( $L = 1\text{ mm}$ ) are overlaid on the corresponding zoomed-in TTTL diagram. Here, despite the proximity of the adopted experimental conditions to the (X+F+A) and (X+F) regions, we were never able to obtain a layered sample; indeed, only fully amorphous, crystalline, and foamed samples are shown.

Nevertheless, new methods to induce layering can be attempted, considering the new picture at hand. Going back to Figure 6a, a higher rate of heat transport can be observed, with a curve that is visibly closer to both the diffusion and crystallization lines. This non-trivial observation allows us to consider the implementation of thermal treatments as an additional means to obtain layering in PET.

A first attempt at this approach is shown in Figure 7b, where the continuous cooling of the PET slab is considered (red arrow). As a consequence of the non-isothermal treatment, the isothermal transformation (TTTL) diagram is no longer valid, and a shift in the crystallization curves must be considered; indeed, the time required for crystallization to occur is delayed during continuous cooling, and the corresponding bell-shaped lines are shifted to longer times and lower temperatures (dashed purple lines)<sup>61</sup>.



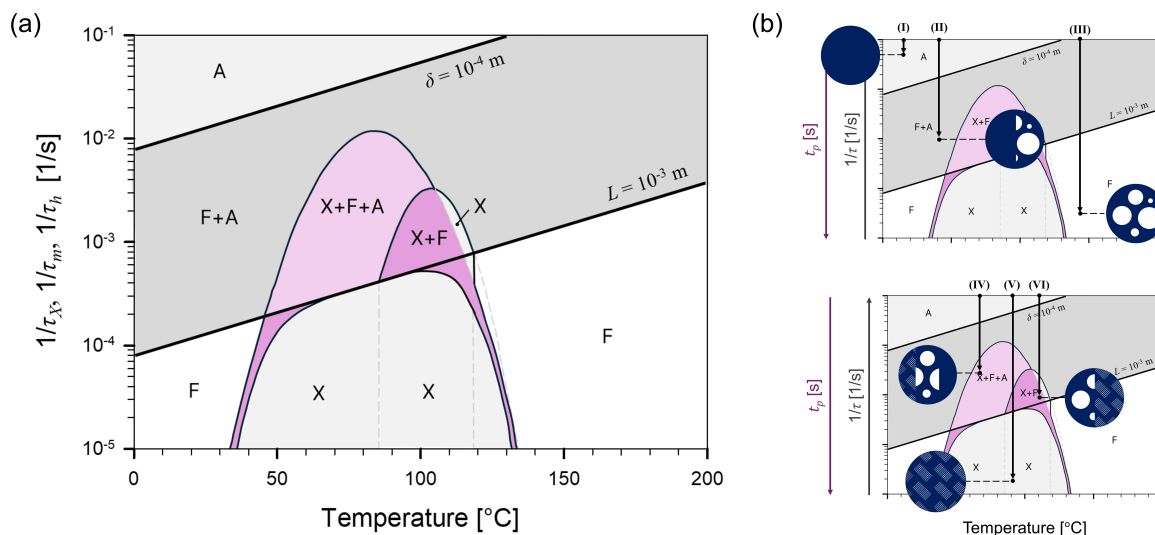


Fig. 3 (a) TTTL diagram for a slab of PLLA ( $L = 1$  mm) treated with  $\text{CO}_2$ . The superimposition of the kinetic curves evidences the presence of six different regions that can help understanding the processing conditions required to obtain a certain morphology: Amorphous (A, light grey), crystalline (X, grey), foamed (F, white), two-layered foamed-amorphous structure (F+A, dark grey), two-layered foamed-crystalline structure (X+F, dark pink) and three-layered foamed-amorphous-crystalline structure (X+F+A, pink). (b) Example of how thermal treatments can be displayed on the TTTL diagram.

The optical micrograph of the cross section of the resulting sample is superimposed on the qualitatively modified graph and shows the effectiveness of this treatment, as a two-layer structure appears. However, a careful and thorough re-thinking of the TTTL diagrams must be considered when dealing with non-isothermal treatments (similarly to what happens in the Continuous Cooling Transformation - CCT - diagrams<sup>61</sup>), to guaranty full comprehension and accurate representation of these processes.

The implementation of this technique is applicable to any type of material processing where a layering within a certain depth  $\delta$  is desired, as long as the following criteria are met: (i) the process involves the transport of mass, momentum, and/or energy (characterized, through  $\delta$ , by a rate  $1/\tau_r$ ); (ii) the process involves a transformation (characterized by a rate  $1/\tau_{1/2}$ ), affected by the transported quantities; (iii) there exist a condition for which  $Da_\delta = \tau_r/\tau_{1/2} \approx 1$ .

Once the potential for layering is established and all the required criteria are met, the TTTL diagram for the system at hand can be built. Starting from the kinetic data for both the transformation and transport phenomena, the evaluation of  $\tau_r$  and  $\tau_{1/2}$  as a function of processing conditions can be exploited to highlight the precise processing window needed to achieve a target layering. The final step requires validation of the theoretically built diagram through a thorough experimental campaign.

## 4 Conclusions

In the present work, we introduce a novel technique to induce material layering in semi-crystalline polymers, specifically referring to the cases of PLLA and PET. We demonstrate that knowledge of the interplay between the numerous transport phenomena happening during physical foaming of a semi-crystalline polymer (heat transport, mass transport and crystallization) is a pow-

erful tool to tailor both foam density and crystallinity distributions in mono-material polymer systems within a single processing step.

Literature data on mass diffusivity, thermal diffusivity and crystallization kinetics of the PLLA/ $\text{CO}_2$  and PET/ $\text{CO}_2$  systems are explored and a more intuitive way of understanding the processing conditions in which semi-crystalline polymers can give a layered structure in the laboratory practice of batch foaming is given. Specifically, the Time-Temperature-Transformation-Layering (TTTL) diagram is presented, with experimental results confirming its effectiveness in predicting the final sample morphology. With this tool at hand, multi-layered foams are obtained, presenting, in the best cases, an amorphous core, a foamed part, and a crystalline skin. The potential of using such graph in any type of material processing in which layering is desired is also foreseen, and the operational pathway to be followed when approaching a new material system is also provided. In this way, the proposed methodology establishes as a fully generalizable framework for processing-driven material structuring.

Future developments may focus on extending the concept to other classes of polymers and reactive systems and to other classes of materials (e.g., metals where Time-Temperature-Transformation diagrams are used, and layering is also a frequent need), further bridging the gap between performance optimization and circular design principles.

## Author contributions

Emilia Di Lorenzo: Writing - original draft, Writing - review & editing, Validation, Methodology, Investigation, Formal analysis, Data curation, Conceptualization, Visualization. Lorenzo Miele: Writing - original draft, Writing - review & editing, Validation, Methodology, Investigation, Formal analysis, Data curation, Con-

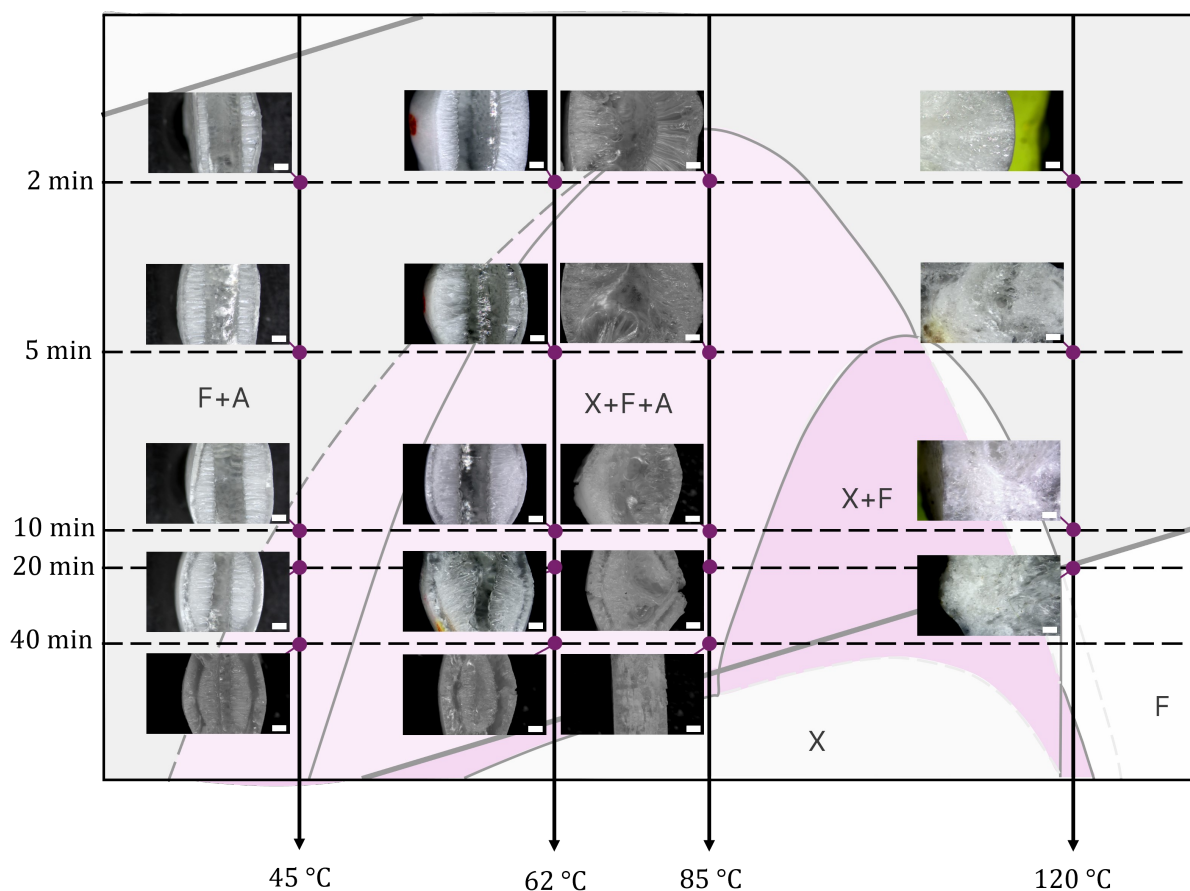


Fig. 4 Microscopy pictures of the cross sections of the PLLA samples ( $L = 1$  mm) treated with 110 bar of  $\text{CO}_2$  at  $T = 45, 62, 85$  and  $120$  °C for a time  $t_p = 2, 5, 10, 20$  and  $40$  min superimposed on the zoomed-in TTTL diagram. The additional dashed black line was added to take into account the fact that we used a higher pressure value for foaming with respect to that found in the literature (45 bar). Concerning the samples treated at  $120$  °C for 2 and 5 min, we decided to only show the foamed part as the samples in their entirety were much bigger than the field of view of the optical microscopy and it was not possible to include both the amorphous and foamed layer in just one microphotography. Scale bar =  $500 \mu\text{m}$ .

ceptualization, Visualization. Alessandra Longo: Writing - review & editing, Conceptualization, Investigation, Project administration, Resources. Ernesto Di Maio: Writing - original draft, Writing - review & editing, Conceptualization, Funding acquisition, Project administration, Supervision, Resources. Maria Laura Di Lorenzo: Writing - review & editing, Conceptualization, Project administration, Funding acquisition, Supervision, Resources.

### Conflicts of interest

The authors declare no competing interests.

### Data availability

Data for this article are available at figshare at <https://figshare.com/s/b1b75594bf0fd1a3adae>.

### Acknowledgements

The authors thank Costantino Casale (University of Naples Federico II) for the support provided in performing the polarized optical microscopy (Figure 2 and Figure 5), Arsenio Cutolo (University of Naples Federico II) for the atomic force microscopy (Figure 2), and Antonio Langella and Massimo Durante (University of Naples Federico II) for the mechanical test. The authors also

warmly thank Total Corbion (Gorinchem, The Netherlands) and Point Plastic (Amasona, Italy) for kindly providing PLLA and PET, respectively.

### Funding declaration

This research was funded by the European Union–Next Generation EU–PNRR M4/C2/INVESTIMENTO.1.1, in the framework of the PRIN 2022 PNRR program (D.D. 1409, 14-9-2022), project n.P20229YNXX “Design for Recyclability: mono-material multi-graded semicrystalline polymer foams” (DesiRe), ERC field PE11, CUP B53D23027510001.

### Notes and references

- 1 J. Wiener, F. Arbeiter, O. Kolednik and G. Pinter, *Materials & Design*, 2022, **219**, 110828.
- 2 T. Magrini, A. Senol, R. Style, F. Bouville and A. R. Studart, *Journal of the Mechanics and Physics of Solids*, 2022, **159**, 104750.
- 3 A. R. Alias, M. K. Wan and N. Sarbon, *Food Control*, 2022, **136**, 108875.
- 4 R. O. Ritchie, *Nature Materials*, 2011, **10**, 817–822.



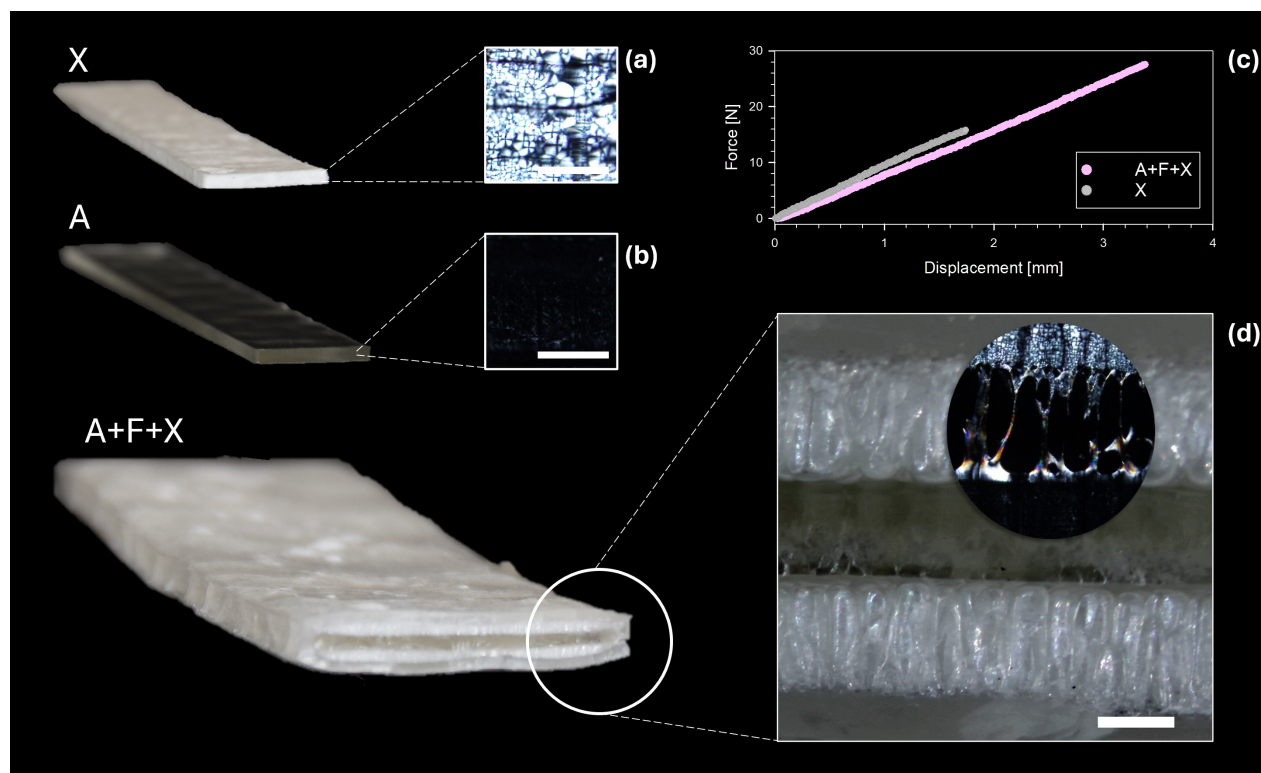


Fig. 5 Crystalline (X), amorphous (A), and layered (X+F+A) PLLA slabs ( $W \times T \times L = 18 \times 2 \times 100 \text{ mm}^3$ ) produced for the three point bending tests through scale up of the already presented process. The corresponding POM micrographs, (a), (b) and (d), respectively, are also presented. Scale bar =  $200 \mu\text{m}$  in (a) and (b), and  $500 \mu\text{m}$  in (d). The force-displacement curves resulting from the three point bending tests on the scaled up crystalline (X) and layered (A+F+X) samples are shown in (c).

- 5 A. Kausar, I. Ahmad, S. A. Rakha, M. Eisa and A. Diallo, *Journal of Composites Science*, 2023, **7**, 102.
- 6 J.-P. Lange, *ACS Sustainable Chemistry & Engineering*, 2021, **9**, 15722–15738.
- 7 L. Shen and E. Worrell, *Handbook of recycling*, Elsevier, 2024, pp. 497–510.
- 8 K. Ragaert, S. Huysveld, G. Vyncke, S. Hubo, L. Veelaert, J. Dewulf and E. Du Bois, *Resources, Conservation and Recycling*, 2020, **155**, 104646.
- 9 M. Guerritore, F. Olivieri, R. Castaldo, R. Avolio, M. Cocca, M. E. Errico, M. R. Galdi, C. Carfagna and G. Gentile, *Resources, Conservation and Recycling*, 2022, **179**, 106126.
- 10 P. Iaccarino, E. Maresca, S. Morganti, F. Auricchio and E. Di Maio, *Advanced Engineering Materials*, 2024, **26**, 2301798.
- 11 J. Zhao, L. Zhang, J. U. Lee, N. D. Sansone, J. Kim, L. Bazbaz, A. A. Faysal and P. C. Lee, *Small*, 2025, **21**, e08472.
- 12 Q. Cheng, L. Jiang and Z. Tang, *Accounts of chemical research*, 2014, **47**, 1256–1266.
- 13 M. Trofa, E. Di Maio and P. L. Maffettone, *Chemical Engineering Journal*, 2019, **362**, 812–817.
- 14 E. Di Lorenzo, F. Romano, L. Ciriaco, N. Iaccarino, L. Izzo, A. Randazzo, P. Musto and E. Di Maio, *Communications Engineering*, 2025, **4**, 1–10.
- 15 E. Di Lorenzo, R. Pasquino, N. Grizzuti and E. Di Maio, *Physics of Fluids*, 2025, **37**, year.
- 16 L. Miele, E. Di Lorenzo, C. Guissart and E. Di Maio, *Heliyon*, 2024, **10**, year.
- 17 A. Longo, E. Di Maio and M. L. Di Lorenzo, *Thermochimica Acta*, 2022, **718**, 179386.
- 18 M. L. Di Lorenzo, *Polymers*, 2024, **16**, 1975.
- 19 A. Longo, E. Di Maio, F. Du, R. Androsch and M. L. Di Lorenzo, *Polymer*, 2023, **285**, 126380.
- 20 M. L. Di Lorenzo, *Macromolecular symposia*, 2006, pp. 176–183.
- 21 M. L. Di Lorenzo, *Journal of applied polymer science*, 2006, **100**, 3145–3151.
- 22 M. L. Di Lorenzo and R. Androsch, *Biodegradable Polyesters*, 2015, 109–130.
- 23 M. L. Di Lorenzo and R. Androsch, *Macromolecular Chemistry and Physics*, 2016, **217**, 1534–1538.
- 24 P. Trucillo, F. Errichiello and E. Di Maio, *Journal of Applied Polymer Science*, 2023, **140**, e54574.
- 25 A. Longo, E. Di Lorenzo, L. Miele, A. Bernardi, E. Di Maio and M. L. Di Lorenzo, *Journal of Polymers and the Environment*, 2026, **34**, 90.
- 26 G. Federico, A. R. Carotenuto, A. Cutolo, M. Fraldi and F. Carlomagno, *Scientific Reports*, 2025, **15**, 18037.
- 27 G. Li, H. Li, L. Turng, S. Gong and C. Zhang, *Fluid Phase Equilibria*, 2006, **246**, 158–166.
- 28 H. Sawada, Y. Takahashi, S. Miyata, S. Kanehashi, S. Sato and K. Nagai, *Transactions of the Materials Research Society of*



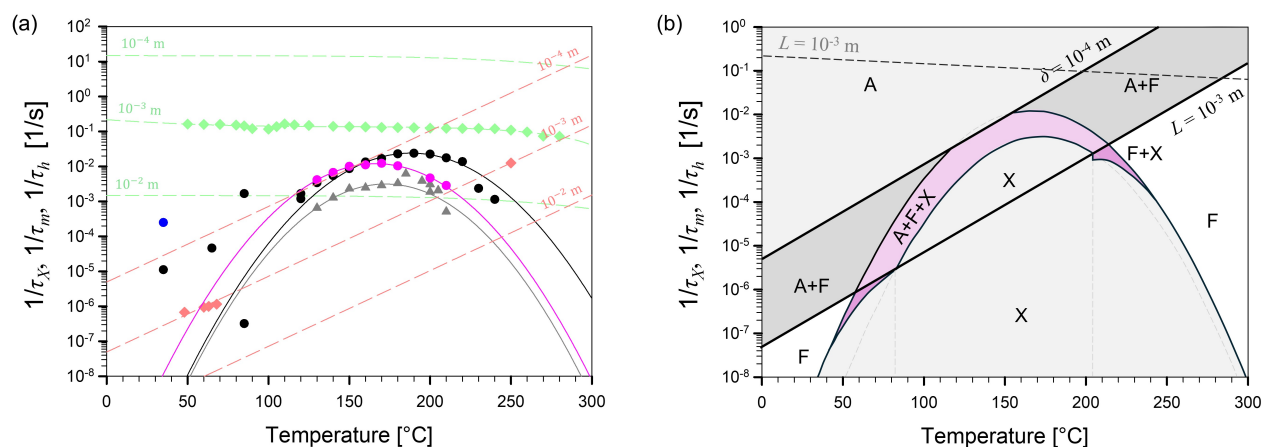


Fig. 6 (a) Comparison of the rates of the three concurring phenomena for the system PET/CO<sub>2</sub>.  $1/\tau_m = D/L^2$  (light red diamonds) is the rate of mass transport<sup>48,54–56</sup>  $1/\tau_h = a/L^2$  (green diamonds) is the rate of heat transport<sup>57</sup>;  $1/\tau_X$  is the crystallization rate. The latter is presented as a function of CO<sub>2</sub> pressure: black, dark blue and blue circles indicate  $1/\tau_X$  at ambient pressure<sup>58,59</sup>, with 50 bar of CO<sub>2</sub><sup>58</sup> and with 60 bar of CO<sub>2</sub><sup>45</sup>, respectively, in the case of cold crystallization; similarly, grey and pink triangles indicate  $1/\tau_X$  at ambient pressure<sup>18,60</sup> and with 60 bar of CO<sub>2</sub><sup>60</sup> in the case of melt crystallization. A value of  $L = 0.1, 1$  and  $10$  mm was used for the evaluation of  $1/\tau_m$  and  $1/\tau_h$ . (b) TTTL diagram for a slab of PET ( $L = 1$  mm) treated with CO<sub>2</sub>. The superimposition of the kinetic curves evidences the presence of six different regions: Amorphous (A, light grey), crystalline (X, grey), foamed (F, white), two-layered foamed-amorphous structure (A+F, dark grey), two-layered foamed-crystalline structure (F+X, dark pink) and three layered foamed-amorphous-crystalline structure (A+F+X, pink). In this case, the heat transport curve is also evidenced (dashed light grey line).

Japan, 2010, **35**, 241–246.

29 K. Yu, H. Zhou, X. Wang, Z. Du and J. Mi, *Journal of Molecular Liquids*, 2019, **280**, 97–103.

30 E. Aionicesei, M. Škerget and Ž. Knez, *The Journal of Supercritical Fluids*, 2008, **47**, 296–301.

31 L. Bai, X. Zhao, R.-Y. Bao, Z.-Y. Liu, M.-B. Yang and W. Yang, *Journal of materials science*, 2018, **53**, 10543–10553.

32 M. Nofar, W. Zhu and C. Park, *Polymer*, 2012, **53**, 3341–3353.

33 H. Tsuji, H. Takai and S. K. Saha, *Polymer*, 2006, **47**, 3826–3837.

34 M. Day, A. Nawaby and X. Liao, *Journal of Thermal Analysis and Calorimetry*, 2006, **86**, 623–629.

35 A. Fernández-Tena, M. Fernández, A. J. Sandoval, M. I. Calafel, A. Aguirre, N. Aranburu, G. Guerrica-Echevarria, M. L. Di Lorenzo, A. Longo, J. F. Vega et al., *International journal of biological macromolecules*, 2024, **282**, 136783.

36 L. Yu, H. Liu, K. Dean and L. Chen, *Journal of Polymer Science Part B: Polymer Physics*, 2008, **46**, 2630–2636.

37 M. L. Di Lorenzo, P. Rubino, R. Luijkx and M. Hérou, *Colloid and Polymer Science*, 2014, **292**, 399–409.

38 M. L. Di Lorenzo, P. Rubino, B. Immirzi, R. Luijkx, M. Hérou and R. Androsch, *Colloid and Polymer Science*, 2015, **293**, 2459–2467.

39 R. Androsch, M. L. Di Lorenzo and C. Schick, *European Polymer Journal*, 2017, **96**, 361–369.

40 R. Androsch, C. Schick and M. L. Di Lorenzo, *Synthesis, Structure and Properties of Poly (lactic acid)*, 2017, 235–272.

41 M. Nofar, A. Tabatabaei and C. B. Park, *Polymer*, 2013, **54**, 2382–2391.

42 M. Nofar, A. Tabatabaei, A. Ameli and C. B. Park, *Polymer*, 2013, **54**, 6471–6478.

43 A. Longo, E. Di Maio and M. L. Di Lorenzo, *Thermochemica Acta*, 2022, **718**, 179386.

44 D.-C. Li, T. Liu, L. Zhao, X.-S. Lian and W.-k. Yuan, *Industrial & Engineering Chemistry Research*, 2011, **50**, 1997–2007.

45 S. Lambert and M. Paulaitis, *The Journal of Supercritical Fluids*, 1991, **4**, 15–23.

46 S. Kadijk and B. Van Den Brule, *Polymer Engineering & Science*, 1994, **34**, 1535–1546.

47 P. Condo, I. C. Sanchez, C. Panayiotou and K. P. Johnston, *Macromolecules*, 1992, **25**, 6119–6127.

48 J. Chiou, J. W. Barlow and D. R. Paul, *Journal of Applied Polymer Science*, 1985, **30**, 2633–2642.

49 R. Pantani, V. Speranza and G. Titomanlio, *European Polymer Journal*, 2017, **97**, 220–229.

50 J. Magill, *Journal of materials science*, 2001, **36**, 3143–3164.

51 R. Aguiar, N. D. Sansone, N. Cheung, A. V. Tuccitto, T. Y. T. Su, I. Soltani, M. Leroux and P. C. Lee, *Advanced Functional Materials*, 2024, **34**, 2403728.

52 D. E. Martínez-Tong, A. Najjar, M. Soccio, A. Nogales, N. Bitinis, M. López-Manchado and T. Ezquerro, *Composites Science and Technology*, 2014, **104**, 34–39.

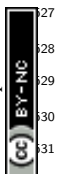
53 G. Molinari, P. Parlanti, L. Aliotta, A. Lazzeri and M. Gemmi, *Materials Today Communications*, 2024, **38**, 107868.

54 A. S. Michaels, W. R. Vieth and J. A. Barrie, *Journal of Applied Physics*, 1963, **34**, 13–20.

55 W. J. Koros and D. R. Paul, *Polymer Engineering & Science*, 1980, **20**, 14–19.

56 L. Sorrentino, E. Di Maio and S. Iannace, *Journal of applied polymer science*, 2010, **116**, 27–35.

57 J. Morikawa and T. Hashimoto, *Polymer*, 1997, **38**, 5397–5400.



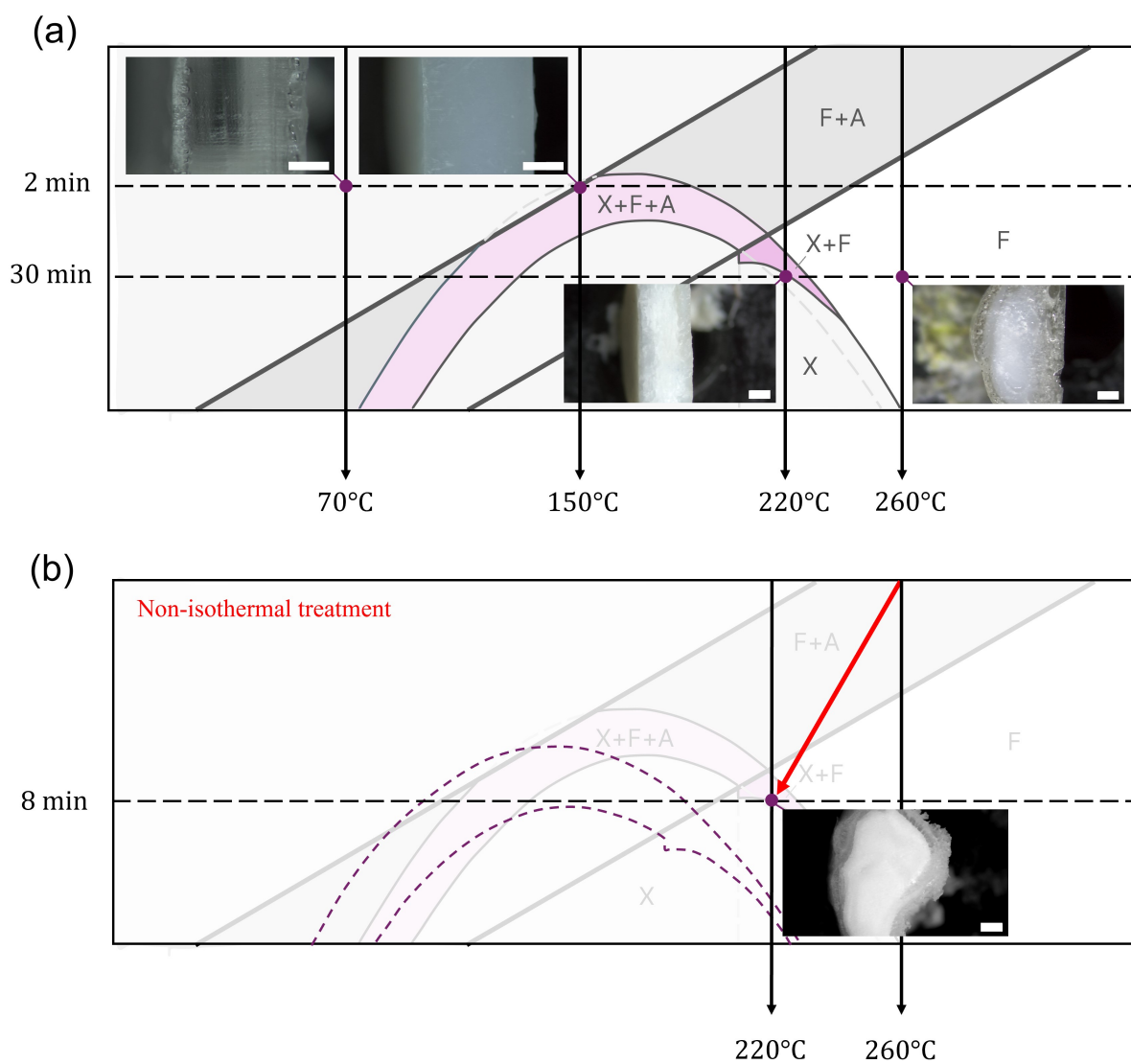


Fig. 7 (a) Optical micrographs of the cross sections of the PET samples ( $L = 1$  mm) treated with 110 bar of CO<sub>2</sub> (a) at a constant temperature of 70, 150, 220 and 260 °C for a time  $t_p = 2$  and 30 min and (b) continuously cooling from 260 to 220 °C for a time  $t_p = 8$  min. In (b), a shift in the bell-shaped crystallization curves as a consequence of the non-isothermal treatment is also qualitatively presented (dashed purple lines). Scale bar = 500  $\mu$ m in both (a) and (b).



- 58 K. Mizoguchi, T. Hirose, Y. Naito and Y. Kamiya, *Polymer*, 1987, **28**, 1298–1302.
- 59 J. Jog, *Journal of Macromolecular Science, Part C: Polymer Reviews*, 1995, **35**, 531–553.
- 60 M. Takada and M. Ohshima, *Polymer Engineering & Science*, 2003, **43**, 479–489.
- 61 W. D. Callister and D. G. Rethwisch, *Fundamentals of materials science and engineering*, John Wiley & Sons, 2022.

